Fuel 383 (2025) 133976

Contents lists available at ScienceDirect

Fuel

journal homepage: www.elsevier.com/locate/fuel

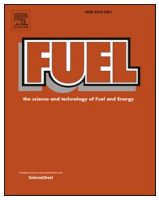

Full Length Article

# Direct reduction of iron ore using biomass biochar: Reduction rate, microstructural and morphological analysis

Antonio Fabozzi [1,*], Francesca Cerciello [1], Osvalda Senneca [*]

*Istituto di Scienze e Tecnologia per l'Energia e la Mobilità Sostenibili (STEMS)- CNR, Italy*

A B S T R A C T

Direct Reduction Iron (DRI) of a natural hematite (Khumani Iron Ore, KIO), by lignocellulosic biomass (Mischantus Giganteous, MIS), has been carried out in a thermogravimetric apparatus (TGA) coupled with evolved gas analysis (EGA) at different temperatures (750–1200 °C) and weight ratios. The microstructural and morphological changes of KIO have been also investigated by means of X-ray Diffraction (XRD) and Scanning Electron Microscopy (SEM).

Biomass pyrolysis is scarcely influenced by the presence of iron up to 500 °C. At higher temperatures, the biochar left behind pyrolysis of biomass acts as reducing agent resulting in progressive reduction from hematite ($Fe_2O_3$) to metallic iron and, in parallel, gasification of the fixed carbon with release of $CO_2$ and mainly CO.

The reduction degree of KIO with biomass turns out to be comparable or even higher than that obtained with gaseous $H_2$ mixtures above ~ 900 °C. XRD shows that $Fe_2O_3$ is completely reduced to metallic iron at 1000 °C. Reduced iron particles show well-developed porosity, with formation of a sponge-like microstructure; EDX metal maps reveal a re-distribution of contaminants in the iron particles after complete reduction. Accumulation of gangue elements, Si, promotes the formation of inorganic rich micro-spheres within the iron sponge-like architecture.

## 1. Introduction

Biomass constitutes a carbon neutral and renewable energy source and has therefore been proposed as substitute of fossil fuels, in particular of coal, in several industrial processes [1,2]. Compared to coal, biomass has the advantage of a much lower ash and sulfur content, and some disadvantages such as higher humidity, lower energy density, lower grindability [3,4]. The properties of biomass can however be adjusted performing appropriate pre-treatments such as drying, torrefaction, hydrothermal carbonization (HTC) or even pyrolysis [5,6].

In order to reduce the carbon footprint of ironmaking, biomass has been proposed as coal substitute for Direct Reduction Iron (DRI) [7,8]. At high temperatures iron ore can be reduced to a molten or sponge by means of blast furnaces process by employing biomass as a reducing agent [9,10]. Biomasses are indeed capable to reduce $Fe_2O_3$ to metallic iron with a relatively high reaction rate and the advantage of low ash production [11,12].

When mixtures of biomass and iron ore processed under controlled atmosphere at high enough temperatures (typically above 800 °C) the first process to occur is pyrolysis of biomass with production of non-condensable products (gas), condensable volatiles (tar), and biochar [13,14]. Biomass and biomass pyrolysis products, biochar and volatile products, can interact with iron ore and promote its progressive reduction to metallic iron [15,16]. At the same time, iron can exert an action on biomass: on one side it can favor the cracking of volatiles, enhancing the yield in gaseous pyrolysis products compared to condensable ones (tar/biooil) [17,18], on the other side, oxides can act as oxygen donors and promote oxidation and gasification of biomass and biomass products, as well known from the literature on chemical looping combustion [19,20].

The kinetics of all these reactive phenomena and their mutual interactions, as well as the yields and properties of gaseous and solid products, deserves attention from the scientific community. Indeed, several papers have investigated the kinetics of DRI with different solid carbonaceous materials, including biomass [21–26]. In particular, some papers focused on reduction kinetics of iron ore with gas produced from biomass pyrolysis [23,24]. Some other papers addressed, instead, the kinetics of reduction by the solid carbon itself [25,26], namely coke or the solid carbon deposited from thermal cracking of biomass volatiles [23].

Guo *et al.* investigated DRI of iron ore by a syngas produced from biomass composite pellets. They report a reduction degree of 88.1 % at 850 °C and 99.95 % at 1050 °C and suggest that the reduction rate is controlled by the chemical reaction at the interface with an activation energy of 104.76 kJ/mol [27]. Similarly, Guo, Dabin *et al.* suggested that the FeO → Fe reaction occurs at the solid–gas interface with an apparent

* Corresponding authors.
*E-mail addresses:* antonio.fabozzi@stems.cnr.it (A. Fabozzi), osvalda.senneca@stems.cnr.it (O. Senneca).
[1] A.F. and F.C. equally contributed to this work.

https://doi.org/10.1016/j.fuel.2024.133976
Received 6 August 2024; Received in revised form 20 November 2024; Accepted 28 November 2024
Available online 1 December 2024

activation energy of 86.05 kJ·mol$^{-1}$ [28].

Zulkania *et al.* studied reduction of iron ore with biomass pellets. In particular, they highlighted the heating rate effect on the reduction reactivity of iron ore-biomass pellets. Indeed, by increasing the heating rate, from 10 to 20 °C/min in temperature range of 600–900 °C an enhancement of the reactivity was observed. Furthermore, the gas analysis showed that carbon gasification becomes relevant at a temperature of 800 °C, thereby increasing the rate of iron ore reduction [29].

Zuo *et al.*, investigated the reduction of iron ore by using different reducing agents such as biomass char (waste wood), coal and coke. In particular, they highlighted that biomass char has the best reduction properties compared to coal and coke. Reduction of $Fe_2O_3$ indeed, occurs at lower temperature with biomass char than with coal and coke, and the maximum reaction rate is 1.57 times higher [30].

Altogether, however, data on the mutual interactions between biomass and iron ores in such a complex reactive system are missing, in particular, both reliable kinetic expressions and detailed information on the physicochemical and structural evolution of iron ore are scarce.

Nevertheless, although great efforts have been made based on the kinetic investigation of DRI using carbonaceous materials, the DRI using a biochar fabricated by biomass pyrolysis one-pot and its kinetic analysis deserves further investigations.

In this scenario, the present work investigates DRI of a natural iron ore (Khumani Iron Ore, KIO) using a raw lignocellulosic biomass, Miscanthus giganteus (MIS), which has been largely investigated as energy source thanks to its potential to produce a large amount of biomass [31]. Miscanthus giganteus (MIS) is indeed an herbaceous feedstock with some features such as highly productive, sterile, rhizomatous, C4 perennial grass and can be considered as a feedstock for bioenergy production. In particular, MIS has been widely investigated and employed in Europe to fabricate electricity and heat *via* combustion. Furthermore, the US government has supported the employment of herbaceous feedstock, in the research activity, for conversion to ethanol for use as transportation fuel.

Microstructural, morphological analysis and kinetic modelling have been explored. In particular, the reduction kinetics of iron ore using the solid product (biochar) as reducing agent, fabricated by MIS pyrolysis, has been studied in order to investigate solid–solid reduction reactions.

Experiments have been carried out in a thermogravimetric apparatus under inert atmospheres at temperatures up to 1200 °C, with different biomass:iron ratios (MIS:KIO). Thermogravimetric analysis has been complemented with evolved gas analysis and with microstructural and morphological analyses of the reduced iron materials, including X-ray Diffraction (XRD) and Scanning Electron Microscopy (SEM). In particular, XRD results have been worked out to calculate the degree of reduction of the iron samples. The rates of mass loss obtained by thermogravimetric analysis have, then, been compared with the reduction rate of KIO from XRD analysis, and furthermore, with the reduction rate of KIO with $H_2$ (assumed as reference), while the evolved gas analysis allowed to address the role of char gasification.

In the framework of the fast-growing field of iron ore-based formulations science and technology, this work represents a first example in which a detailed investigation of the iron ore-based materials reduced with biomass, gives a reliable basis to link the functional behavior of biomass/iron ore formulations to their microstructure and to the fast understanding of their kinetic investigations in order to produce a functional materials for ironmaking industry.

## 2. Materials and methods

KIO and MIS in the sieve fraction of 90–200 μm were employed. Raw materials were provided by the laboratory of industrial chemistry, Ruhr University Bochum (RUB). KIO is a natural iron ore used in [32]. α-alumina (was purchased at Sasol, Italy, and used as a standard (10 wt %) for a quantitative XRF analysis. Proximate and Ultimate analyses on MIS were performed using a LECO TG701 and a LECO CHN 628 according to the standard procedures ASTM D5142 (UNI 9903) and ASTM D 5373, respectively. The results of the analyses (average over 3–5 measures) are reported in Table 1.

Metal components of KIO and MIS were determined *via* X-Ray Fluorescence (XRF) [33,34], using a Nexde-Rigaku instrument. In particular, crystalline α alumina was used as an internal standard and the weight fraction (wt%) of each oxide that composes KIO was determined and reported in Table 2**,** while a qualitative analysis of MIS metal components is reported in **Table S1**.

KIO and MIS at different weight ratios were mixed by means of a vortex for 2 min at 250 rpm at 25 °C obtaining the weight ratios reported in Table 3.

The weight fractions for MIS:KIO formulations were chosen in order to obtain the DRI, ($Fe_2O_3 \rightarrow Fe$). In particular, the 3:1 MIS:KIO sample was first prepared and treated at different temperatures, as reported in Table 3. Subsequently, once the optimal temperature conditions were found, the amount of MIS was gradually decreased and investigated at all chosen temperatures in order to determine the best formulation, MIS:KIO, to obtain the DRI.

The thermal behavior of the different MIS:KIO mixtures was studied in a thermobalance (NETZSCH 409CD). Approximately 60 mg of sample were used for each test. Samples were heated up to the final temperature T, between 750–1200 °C, in a flow of nitrogen of 200 ml/min (STP) with a constant heating rate of 10 °C/min. The final temperature was held for 2 h. The CO, $CO_2$ and $CH_4$, released throughout the TGA runs were measured online by gas analyzers ABB AO2020 (*Uras 26*). Double determinations have been performed to ensure the reproducibility of the results. Samples are labelled as *x:y T,* where *x* is the weight ratio of MIS, *y* is the weight ratio of KIO and *T* is the final temperature of the TG experiments. For example, the sample made of 50 wt% of MIS, 50 wt% of KIO and treated up to 750 °C in TG is labelled *1:1 750 °C*.

The mass recorded during TGA experiments was worked out in order to obtain TG and DTG plots of ($m/m_o$) and ($dm/dt/m_o$) vs. *time*, where and $m$ and $m_0$ are the actual and the initial weight of the sample.

The mass recorded during TGA experiments was worked out in order to obtain:

- DTG curves of derivative mass loss $\frac{1}{m_0}\frac{dm}{dt}$ versus time where and $m$ and $m_0$ were the actual and the initial weight of the sample.
- instantaneous reaction rate curves of $dx/dt$ versus $x$ , with conversion $x$ defined as $x = \frac{m_0 - m}{m_0 - m^*}$ where $m$ and $m_0$ are the actual and the initial weight of the sample, while $m_*$ is the weight at of the TG experiment at 500 °C. This conversion rate includes biomass pyrolysis.
- Instantaneous reaction rate curves of $dx^*/dt$ versus $x^*$, with conversion $x^*$ defined as $x^* = \frac{m^* - m}{m^* - m_f}$ where $m^*$ is the weight of the sample at 500 °C, while m and $m_f$ are still the actual and final samples weight. This conversion rate neglects the initial stage of biomass pyrolysis and refers, mainly, to iron oxides reduction
- the non-isothermal TGA data have been worked to obtain Arrhenius plots of $\ln\left(\frac{dx}{dt}\frac{1}{1-x}\right)$ or $\ln\left(\frac{dx^*}{dt}\frac{1}{1-x^*}\right)$ versus 1/T.

Analysis of reduced samples for has been performed by SEM FEI Ispect S, Column E-SEM W, Source: 200 V–30 KV, filament: tungsten equipped with an Everhart–Thornley detector (ETD).

**Table 1**
Ultimate analysis of MIS (dry basis; *by difference).

| $C_{d.b.}$ wt% | $H_{d.b.}$ wt% | $N_{d.b.}$ wt% | O wt%* |
|---|---|---|---|
| 43.3 | 5.81 | 0.27 | 50.62 |
| Moisture wt% | Volatile wt% | Fix Carbon wt% | Ash wt% |
| 4.7 | 67.6 | 20.5 | 7.2 |

**Table 2**
Quantitative XRF analysis of KIO.

| Sample | Metal Oxide Components wt% | | | | | | | | |
|---|---|---|---|---|---|---|---|---|---|
| | $Fe_2O_3$ | $SiO_2$ | $Al_2O_3$ | $K_2O$ | MgO | MnO | $TiO_2$ | $P_2O_5$ | CaO |
| KIO | 85.7 | 3.2 | 3.8 | 0.05 | 0.15 | 0.22 | 0.08 | 0.28 | 0.04 |

**Table 3**
Different weight ratios of MIS:KIO formulations investigated at different final temperatures.

| MIS:KIO (wt%) | Final temperature (°C) | | | |
|---|---|---|---|---|
| | 750 | 900 | 1000 | 1200 |
| 1:2 | | | x | |
| 1:1 | x | x | x | |
| 2:1 | x | x | x | |
| 3:1 | x | x | x | x |

Microstructural investigations were carried out by means of X-Ray powder Diffraction (XRD) analysis in the 2Θ range 3-90° using a Rigaku Miniflex 600 automated diffractometer equipped with a CuKα radiation source. Phases were identified by using the PDF-5 + 2024 database (ICDD International Centre for Diffraction Data®, Newtown Square, PA, USA) and the Rigaku Smart Lab II software v4.5.162.0. The determination of Indices Refraction Ratio (RIR) was performed without considering the amorphous phase.

## 3. Results and discussion

### 3.1. Microstructural investigations

Microstructural and morphological investigation of samples at different MIS:KIO ratios treated at different temperatures with $N_2$ has been performed by XRD and SEM and EDX.

Results of the structural investigation carried out by XRD on different MIS:KIO mixtures treated at 750 °C (blue), 900 °C (red) and at 1000 °C (black) are reported in Fig. 1.

Microstructural investigations carried out by XRD on different MIS:KIO ratios treated at different temperatures are reported in Fig. 1, while XRD pattern of MIS:KIO (3:1) treated at 1200 °C, is reported in **Fig. S1**.

The XRD pattern of the MIS:KIO 1:1 treated at 750 °C shows diffraction peaks (labelled as 1) corresponding to crystalline phases of the $Fe_3O_4$ and FeO (labelled as 3) with a minor diffraction peak attributable to the $SiO_2$ (labelled as 2), Fig. 1a. By increasing the temperature from 750 to 900 °C at constant MIS:KIO ratios, a conversion of $Fe_3O_4$ → FeO and of FeO → Fe present in two different crystalline phases (labelled as 4 and 5) is detected. However, the further increase in temperature leads to a total conversion of FeO into the two crystalline phases of Fe which are composed of Fe and αFe. Conversely, by increasing the MIS:KIO ratio from 1:1 to 2:1, Fig. 1b, the treatment at 750 °C showed different crystalline phases composed of $Fe_3O_4$ and FeO. Further increasing the temperature from 750 °C to 900 °C a gradual conversion of $Fe_3O_4$ → FeO → Fe occurs. At 1000 °C with a MIS:KIO ratio of 3:1 wt %, two crystalline phases can be observed, namely Fe and αFe. The presence of these two crystalline phases is probably attributable to the possibility of liquid crystalline phases formation between the tar, deriving from MIS pyrolysis and Fe. Formation of a liquid crystalline phases, as described by Shibata *et al.*, between Fe-C is verified at temperature higher than 1200 °C [35,36]; however, the formation of the probably liquid crystalline phases already at 1000 °C may be due to the presence of silica (Si is present in both KIO, ~5%, and MIS, ~34 % as reported by XRF analysis).

In order to determine the wt% of all crystalline phases RIRs of the MIS:KIO samples treated at different temperatures are reported in Table 4.

From the inspection of the Table 4 it is possible to observe that the $Fe_2O_3$ → $Fe_3O_4$ → FeO → Fe reaction progresses by increasing both the MIS:KIO ratios and temperatures.

XRD results have been further used to determine the reduction de-

**Table 4**
RIRs of the MIS:KIO samples treated at different temperatures.

| RIR (wt%) | | | | |
|---|---|---|---|---|
| | $Fe_3O_4$ | FeO | Fe | αFe |
| 1:1 750 °C | 33 | 62 | | |
| 2:1 750 °C | 31.7 | 67.3 | 1 | |
| 3:1 750 °C | 72 | 15 | 1 | 1.5 |
| 1:1 900 °C | | 38 | 9 | 44 |
| 2:1 900 °C | | 28 | 6 | 66 |
| 3:1 900 °C | | 18 | 4 | 68 |
| 1:2 1000 °C | | | 15 | 75 |
| 1:1 1000 °C | | | 10 | 80 |
| 2:1 1000 °C | | | 5 | 85 |
| 3:1 1000 °C | | | 3 | 87 |
| 3:1 1200 °C | | | 2 | 88 |

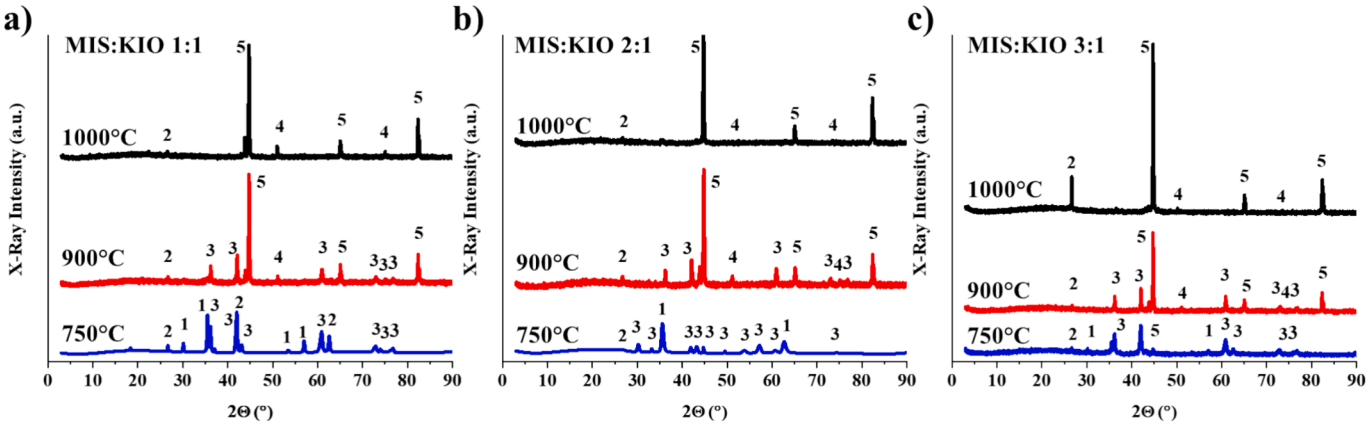


**Fig. 1.** XRD pattern of different MIS:KIO ratio treated at different temperatures. The crystalline phases, with ICDD codes, are indicated: 1 = $Fe_3O_4$, 01–088-0866; 2 = $SiO_2$, 01–089-8937; 3 = FeO, 01–073-2144; 4 = Fe, 01–089-7194; 5 = αFe, 01–080-3816. (For interpretation of the references to color in this figure legend, the reader is referred to the Web version of this article).

gree as a function of the MIS:KIO ratios and temperatures; not taking into account the 10 % of the crystalline phase composed of residual $SiO_2$ which is stable at all temperatures investigated. In particular, the reduction degree was determined according to O/Fe amount, by using the following **Eqs. (1)–(2)**. Results are reported in Fig. 2:

$$\frac{O}{Fe} = \frac{\%wtFe_2O_3 x \frac{O}{Fe} + \%wtFe_3O_4 x \frac{O}{Fe} + \%wtFeOx \frac{O}{Fe}}{100} \quad (1)$$

$$RD = \frac{\frac{O}{Fe}s - \frac{O}{Fe}}{\frac{O}{Fe}s} x100\% \quad (2)$$

where in the $\frac{O}{Fe}$ equation %wt of $Fe_2O_3$, $Fe_3O_4$ and FeO are the weight percentages obtained by XRD characterization, $\frac{O}{Fe}$ are the components of each phase, while in RD $\frac{O}{Fe}s$ represents the ratio of the starting materials ($Fe_2O_3$) while $\frac{O}{Fe}$ is calculated as previously mentioned.

From the inspection of Fig. 2 it is possible to observe that at 750 °C the reduction degree of KIO ($Fe_2O_3 \rightarrow Fe$) increases along with MIS:KIO ratios. However, a complete KIO reduction at 750 °C is not achieved, as it is possible to observe also from Table 4. This trend is observed even at 900 °C where the reduction degree is higher than 750 °C for all weight ratios investigated; however, a complete DRI was not obtained because FeO crystalline phases are still detected, Fig. 1. Contrariwise, a complete reduction DRI of KIO is obtained at 1000 °C for all MIS:KIO ratios in which the RD is ~ 100 %.

### 3.2. Thermogravimetric and gas analysis

Fig. 3 shows the TG-DTG and gas release curves of MIS pyrolysis up to 900 °C.

The TG-DTG curves in Fig. 3a show that two main stages of pyrolysis take place between 250–500 °C, accounting for 68 % of mass loss. Pyrolysis tail above 500 °C accounts for less than 5 % of weight loss. The gas profiles in Fig. 3b consistently show two well resolved and comparable CO and $CO_2$ peaks before 500 °C. The $CH_4$ peak is shifted by approximately 50 °C, but its height is remarkably low compared to that CO and $CO_2$. Notably also $H_2$ profiles were recorded (**Fig. S2**), but the concentration was so low to be considered negligible.

Fig. 4 reports the TG-DTG curves of experiments with MIS and KIO at different weight ratios and temperatures between 750 and 1000 °C. The profiles of CO, $CO_2$ and $CH_4$ formed during the TG tests are reported in Fig. 5. The TG-DTG and gas profiles obtained at 1200 °C with the MIS:KIO ratio of 3:1 are reported in Fig. 6.

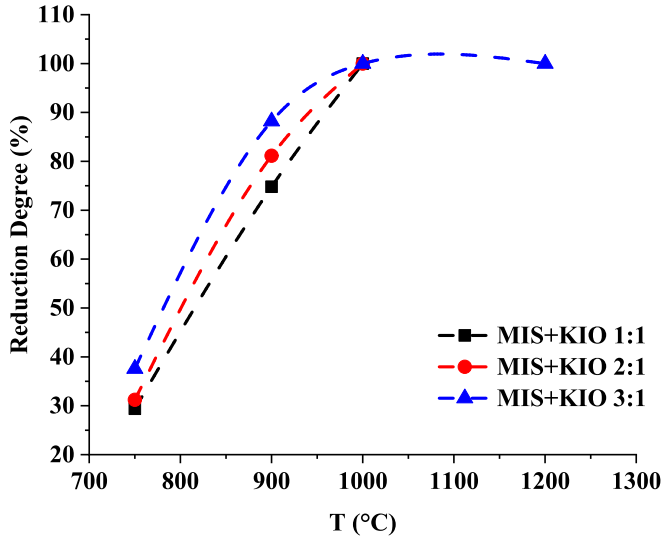


**Fig. 2.** Reduction degree of KIO by using MIS at different both MIS:KIO ratios and temperatures.

As already mentioned above for experiments on MIS alone, the $H_2$ profiles were recorded (**Fig. S2**), but the concentration was so low that its relevance to the observed phenomenology was considered negligible.

It can be observed that for all the conditions investigated, the two stages of MIS pyrolysis before 500 °C are not affected by the presence of KIO. The weight loss up to 500 °C corresponds to what expected from pyrolysis of the MIS fractions, and no shift is observed in the DTG peaks (390 °C). Another well resolved stage of weight loss is observed for 750 °C < T < 1000 °C, most likely attributable to KIO reduction. In the intermediate temperature (500–750 °C), the weight loss is relatively modest, however in this region MIS pyrolysis tails and initial stages of KIO reduction may overlap and even interfere with each other and a clear distinction between reactive phenomena is not possible.

For T < 500 °C (t < 50 min), the production of CO, $CO_2$ and $CH_4$ is attributed to the light gases generated during biomass pyrolysis. The addition of KIO does not shift the gas release peaks up to 500 °C (XRD pattern is reported in **Fig. S3**). For T > 750 °C further peaks of CO, $CO_2$ are detected. This effect is even stronger at 1000 °C for all MIS:KIO weight ratios.

From Fig. 6 it can be observed that when the temperature is further raised to 1200 °C, an even later peak of CO is observed, which parallels with an additional DTG peak.

The presence of other peaks of CO at high temperature, T > 700 °C is attributed mainly to Boudouard reaction, as will be better discussed in the paragraph on "mass balances". A contribution to CO release from reactions involving other metals, cannot, however, not be excluded a priory, since the starting material ($Fe_2O_3$) contains also other metals, Table 2, and are not detected from XRD, and could in principle result in eutectics [37].

### 3.3. Mass balances

Tables 5–6 report the results of mass balances carried out on TG and evolved gas analysis.

The overall mass loss due to gaseous products has been calculated as follows:

$$\left(\frac{m}{m_{0,MIS}}\right)_{Gas} = \frac{MIS + KIO}{m_0 MIS}\frac{Q}{V_m}\int_{t_0}^{t^*} 28COdt + \int_{t_0}^{t^*} 44CO_2dt + \int_{t_0}^{t^*} 16CH_4dt \quad (3)$$

$$\left(\frac{m}{m_{0,KIO}}\right)_{Gas} = \frac{MIS + KIO}{m_0 KIO}\frac{Q}{V_m}\int_{t^*}^{t_f} 28COdt + \int_{t^*}^{t_f} 44CO_2dt + \int_{t^*}^{t_f} 16CH_4dt \quad (4)$$

Where $Q$ is the gas flow rate used in the TG experiment, $V_m$ (= 22.4 L/mol) is the volume of one mole of ideal gas at standard temperature and pressure, CO, $CO_2$, $CH_4$, and $CO_0$, $CO_{2_0}$, $CH_{4_0}$ are the molar fractions of the gas products measured by gas analyzers at any time $t$ and at the beginning of the test. As far as the time intervals are concerned, two calculation sets have been carried out: from the beginning of the heat up, till the time t* when the temperature of 500 °C is reached, and from this time to the end of the experiments (when cooling down starts). This has been done because, at 500 °C within a first order approximation, biomass pyrolysis can be considered almost complete, while iron ore reduction can be considered negligible. Therefore, for the first-time interval, when pyrolysis of biomass dominates, data have been normalized with respect to the mass of MIS, $m_{0,MIS} = m^*_{0\frac{MIS}{(MIS+KIO)}}$, whereas for the second interval (above 500 °C) the data have been normalized with respect to the mass of the KIO loaded in the experiment, $m_{0,KIO} = m^*_{0\frac{KIO}{(MIS+KIO)}}$.

From the overall mass balances in Table 5 it can be observed that the mass loss with light gases in the pyrolysis stage (below 500 °C) is smaller than the corresponding weight loss measured by the thermobalance. This is not surprising because CO, $CO_2$, $CH_4$ (and $H_2$) are only a fraction

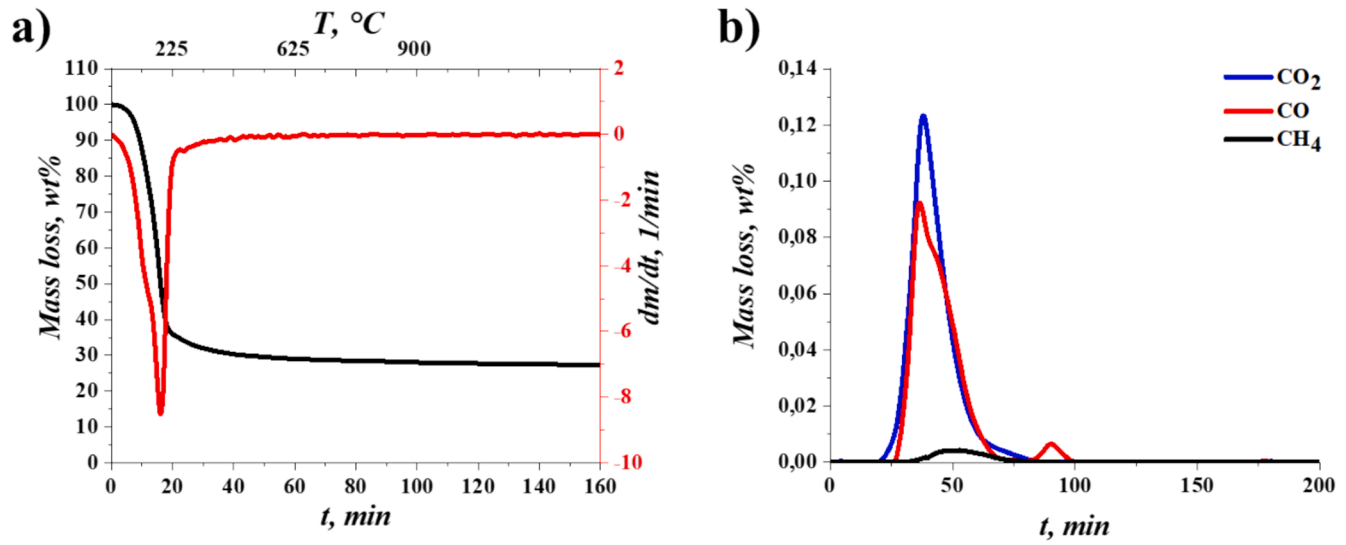


**Fig. 3.** TG-DTG and gas release curves of MIS pyrolysis up to 900 °C.

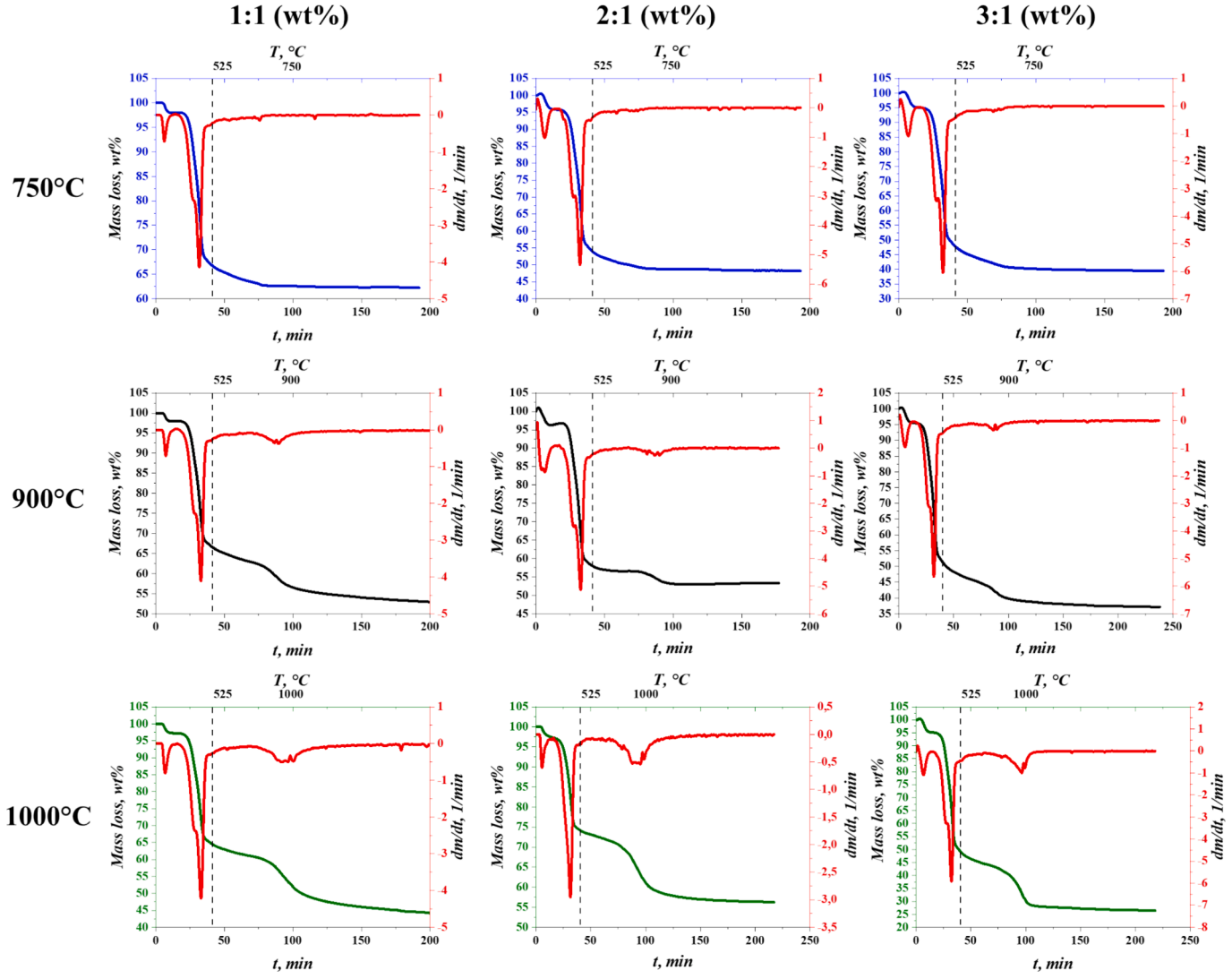


**Fig. 4.** TG-DSC curves of the MIS:KIO at different ratios and at different temperatures under $N_2$ atmosphere.

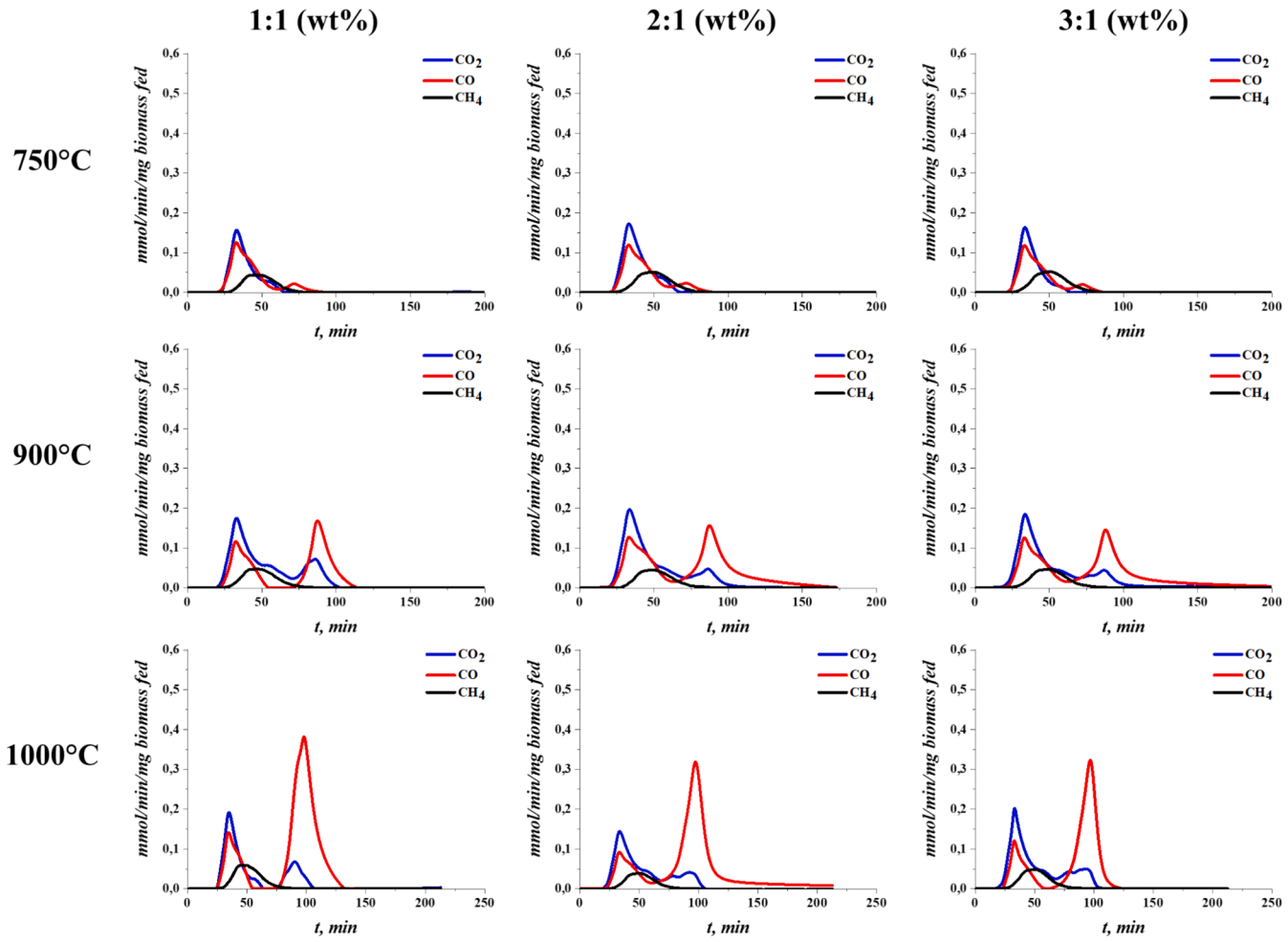


**Fig. 5.** Gas release curves at different KIO:MIS weight ratios and at different temperatures.

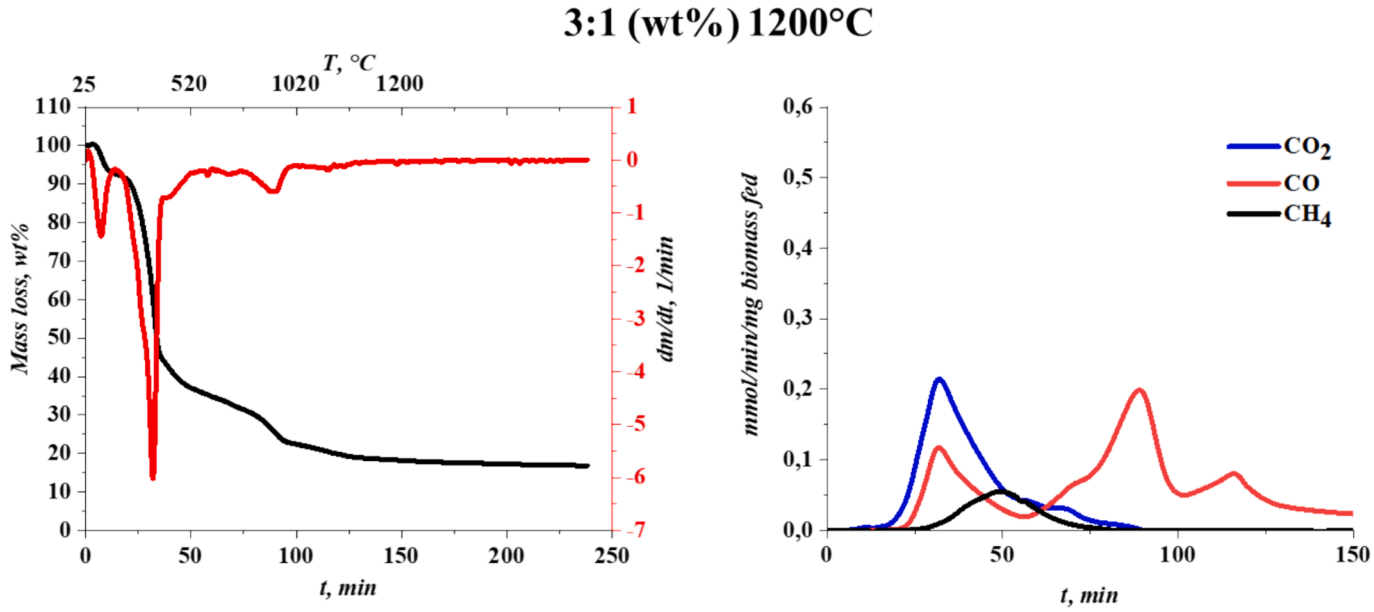


**Fig. 6.** TG-DTG and Gas release curves of MIS:KIO 3:1 (wt%) at 1200 °C.

**Table 5**
Mass balances carried out on TG and evolved gas analysis; (1 wt% calculated respect to weight of the biomass loaded; 2 wt% calculated respect to weight of the iron ore loaded).

| | | MIS | 1:1 750 °C | 2:1 750 °C | 3:1 750 °C | 1:1 900 °C | 2:1 900 °C | 3:1 900 °C | 1:2 1000 °C | 1:1 1000 °C | 2:1 1000 °C | 3:1 1000 °C | 3:1 1200 °C |
|---|---|---|---|---|---|---|---|---|---|---|---|---|---|
| Pyrolysis T < 500 °C | %wt lost $TG^1_{Biomass\ normalized}$ | 68.2 | 64.6 | 68.4 | 66.3 | 65.2 | 82.4 | 97.6 | 75 | 70 | 67.5 | 69.3 | 78. 7 |
| | %wt $gas^1_{Biomass\ normalized}$ | 11.2 | 11.2 | 12.5 | 13.8 | 12.3 | 14.4 | 14.2 | 13.2 | 13.2 | 12.8 | 15.5 | 18.5 |
| Reduction T ≥ 500 °C | %wt lost $TG^2_{KIO\ normalized}$ | | 8.2 | 9.9 | 16.4 | 12.2 | 37.5 | 48 | 25.5 | 50 | 63 | 84 | 92 |
| | %wt $gas^2_{KIO\ normalized}$ | | 4.6 | 12 | 17.2 | 16.2 | 38.4 | 54 | 25.3 | 46 | 57 | 80 | 84 |

**Table 6**
Mass balance at T ≥ 500 °C of different temperatures and MIS:KIO weight ratios.

| Molar ratios | 1:1 750 °C | 2:1 750 °C | 3:1 750 °C | 1:1 900 °C | 2:1 900 °C | 3:1 900 °C | 1:2 1000 °C | 1:1 1000 °C | 2:1 1000 °C | 3:1 1000 °C | 3:1 1200 °C |
|---|---|---|---|---|---|---|---|---|---|---|---|
| $C_{gas}/C^*$ | 0.09 | 0.11 | 0.12 | 0.25 | 0.33 | 0.30 | 0.84 | 0.75 | 0.51 | 0.47 | 0.50 |
| $O_{KIO}/C^*$ | 0.52 | 0.26 | 0.17 | 0.52 | 0.26 | 0.17 | 1.05 | 0.52 | 0.26 | 0.17 | 0.17 |
| α | 0.60 | 0.55 | 0.66 | 0.53 | 0.68 | 0.67 | 0.69 | 0.70 | 0.78 | 0.70 | 0.80 |

of the volatiles produced by biomass pyrolysis. Especially in the early stages of pyrolysis a multitude of hydrocarbon species are released, including gaseous species with more than two carbon atoms ($C_2$-$C_6$), and heavier hydrocarbons (tars) which have not been analyzed in the present work [38]. Notably, when the temperature and the biomass to iron ore ratio increase, the yield of light gases increases moderately, suggesting that part of the heavy pyrolysis products (TAR) may undergo cracking (resulting in higher $CH_4$ concentration) because of catalytic effect of KIO.

In the second stage, above 500 °C, the weight loss increases progressively with temperature and MIS:KIO ratios. Notably data has been normalized with respect to the KIO content. When the $Fe_2O_3$ is completely reduced to metallic iron, it loses 30 % of its mass. Therefore, if only the reduction of iron took place above 500 °C, the maximum allowed values in Table 5 should be 30 %. Instead, when the temperature exceeds 900 °C, for high enough MIS:KIO ratios, much larger weight loss is obtained. This clearly indicates that in the temperature range above 500 °C biomass gasification occurs in parallel with KIO reduction. Carbon gasification explains also the late CO peaks shown in the gas profiles curves of Fig. 4.

The temperature range above 500 °C has been further investigated by looking at the mass balances on carbon. The overall reaction for KIO reduction and carbon oxidation is considered to occur above 500 °C, Eq. (5):

$$Fe_2O_3 + \frac{3}{2-\alpha}C \rightarrow 2Fe + \frac{3}{2-\alpha}\alpha CO + \frac{3}{2-\alpha}(1-\alpha)CO_2 \quad (5)$$

The CO, $CO_2$ and overall carbon loss as gaseous species above 500 °C was calculated according to the following equations:

$$\left(\frac{C_{CO}}{C^*}\right)_{mol} = \frac{1}{C^*}\frac{Q}{V_m}\int_{t^*}^{t_f} CO\,dt \quad (6)$$

$$\left(\frac{C_{CO_2}}{C^*}\right)_{mol} = \frac{1}{C^*}\frac{Q}{V_m}\int_{t^*}^{t_f} CO_2\,dt \quad (7)$$

$$\left(\frac{C_{gas}}{C^*}\right)_{mol} = \frac{1}{C^*}\frac{Q}{V_m}\int_{t^*}^{t_f} (CO + CO_2 + CH_4)\,dt \quad (8)$$

Here $t^*$ is the time when temperature reached 500 °C and $t_f$ is the time at the end of the experiment. Notably, the C* is the molar carbon content of the sample at 500 °C, which can be roughly considered the fixed carbon of the biomass. Based on the TG results on MIS and on its proximate analysis, $C^*$ has been calculated as $C^* = m_0\left(\frac{MIS}{MIS+KIO}\right)\frac{0.23}{12}$, where $m_o$ is the total mass of sample (KIO + MIS) loaded at the beginning of the experiment.

Results of the overall carbon loss, from 500 °C till the end of the experiment are reported in Table 6, together with the values of $\alpha = \frac{CO}{CO+CO_2}$.

From the inspection of Table 6**,** it emerges that for the fixed MIS:KIO ratios of 1:1, the fraction of fixed carbon which is oxidized (above 500 °C) increases progressively with the final reaction temperature, while for a fixed temperature it decreases with increasing MIS:KIO ratios.These results can be explained by the fact that, even when temperature was high enough to reduce $Fe_2O_3$, the amount of KIO was insufficient to oxidize all the fixed carbon present in the biomass.

In fact, the molar ratios of $O_{KIO}/C^*$ are also reported in the table, where $O_{KIO}$ is the total content of elemental oxygen present in the loaded sample, calculated as $O_{KIO} = m_0\left(\frac{KIO}{MIS+KIO}\frac{1}{156}\frac{3}{2}\right)$.

It can be observed that carbon was in excess with respect to KIO $\left(\frac{O_{KIO}}{C^*} < 1\right)$ in all the tests, with the only exception of the test carried out with MIS:KIO ratio of 1:2, which was indeed the case with the highest conversion of fixed carbon ($C_{gas}/C^*$=0.84).

As far as the overall stoichiometry of the reaction is concerned, the value of $\alpha = \frac{CO}{CO+CO_2}$, reported in Table 6**,** increases with temperature, reaching values of 0.7–0.8 above 1000 °C, where reduction of KIO to Fe is complete. Notably the result is consistent with the thermodynamic considerations reported in [23] which show that at 1000 °C with α values of 0.7 the stable iron form is Fe.

### 3.4. Role of biochar in KIO reduction

It is important to understand if the reduction of KIO can be attributed to (solid–solid) reaction of KIO with the biochar formed in the pyrolysis stage, or rather it should be attributed to (gas–solid) reaction of KIO with

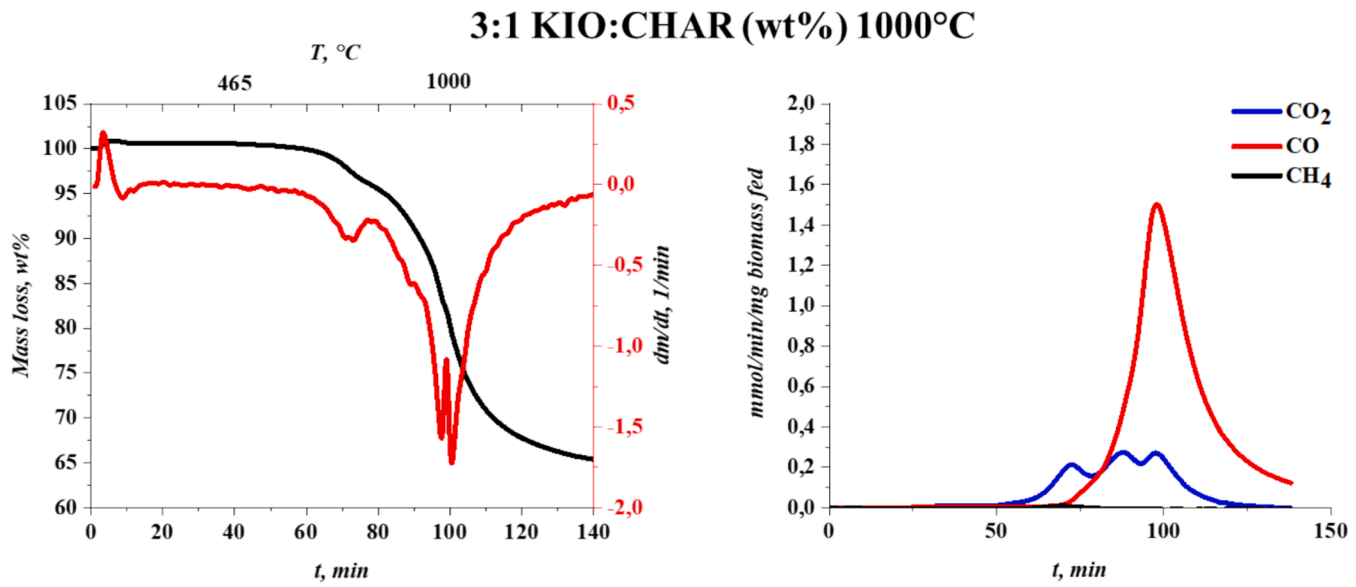


**Fig. 7.** TG and gas release curves of KIO:CHAR (MIS) 3:1 wt% at 1000 °C.

the volatile products of biomass pyrolysis. For this reason, biochar from MIS was produced at 600 °C in TG in a flow of $N_2$ and 10 °C/min heating rate. KIO was then mixed with the char with the weight ratio 3:1 and treated at 1000 °C in the TGA, Results are shown in Fig. 7.

The TG curve shows that the weight loss starts only above 700 °C in correspondence of the release of the first peak of $CO_2$. For T > 870 °C, the reaction proceeds with the release of 3 peaks of $CO_2$ and one remarkable release of CO. These results confirm the prevalent role of biochar's fixed carbon on reduction of KIO. The three stages of reaction might be associated with the three-reduction stapes: $Fe_2O_3 \rightarrow Fe_3O_4 \rightarrow FeO \rightarrow Fe$. The Boudouard reaction contributes to the large formation of CO at T > 700 °C.

Notably, even though in the present set up, the contribution of volatiles to overall reduction of KIO was small compared to that of char, the situation could be different in an industrial scale up where volatiles and iron ores are in more prolonged contact at high temperature than in the present work [39].

### 3.5. Kinetic analysis

Arrhenius plots have been calculated for assuming a simple kinetic law, as reported in the following equations:

$$\frac{dx}{dt} = k_0 \exp^{\frac{-E_a}{RT}}(1-x) \quad (9)$$

$$\frac{dx^*}{dt} = k_0 \exp^{\frac{-E_a}{RT}}(1-x^*) \quad (10)$$

where x is the conversion degree, $k_0$ the pre-exponential factor, the activation energy ($E_a$) and $R$ the gas constant.

Example of the Arrhenius plots obtained from the sample with MIS:KIO weight fraction of 1:1 at 1000 °C is reported in Fig. 8.

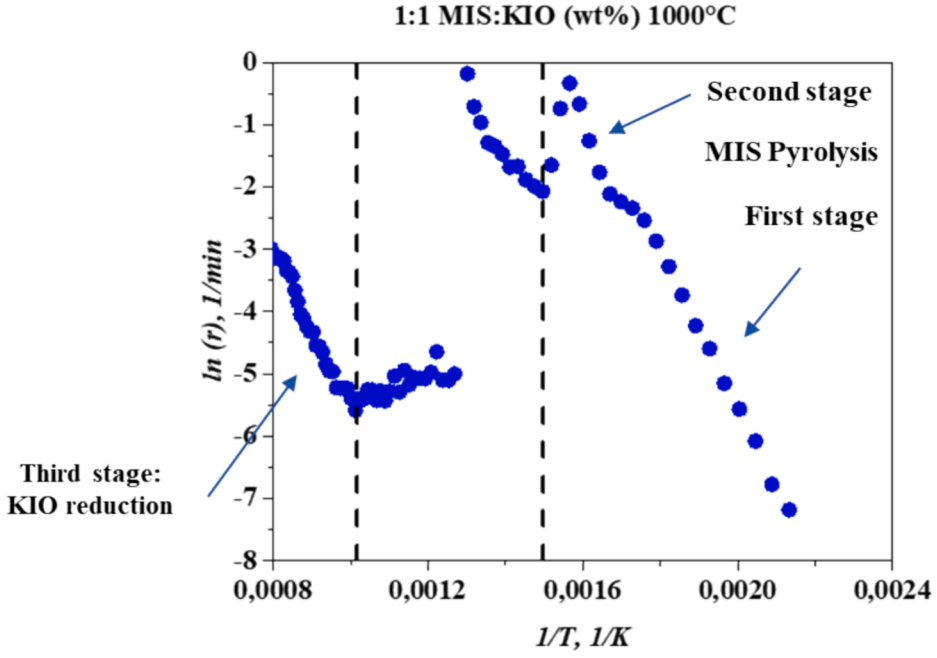


**Fig. 8.** Arrhenius plots of 1:1 MIS:KIO at 1000 °C.

It can be noted that the Arrhenius plot in the low temperature range exhibits two linearity ranges which correspond to the two main stages of biomass pyrolysis. In the intermediate temperature range the overlapping of pyrolysis tails and early reduction stages makes it difficult to obtain reliable kinetic data. Another linearity range can be well identified, instead, for T > 750 °C. The latter could be attributed to the reduction of KIO with biochar and the kinetic parameters obtained by linear fitting are reported in Table 7.

The reported value of $E_a$ can be compared and discussed against available results from other research groups [40–43]. Some papers on reduction of iron oxides in mixtures with carbon (also known as self-reduction) report values of the order of 300–450 kJ/mol [44,45], much higher indeed than the one obtained in the present work. Such high activation energy was explained within the two-step reaction mechanism:

$$Fe_xO_{y(s)} + CO_{(g)} \rightleftarrows Fe_xO_{y-1(s)} + CO_{2(g)} \quad (11)$$

$$C_{(s)} + CO_{2(g)} \rightleftarrows 2CO_{(g)} \quad (12)$$

Accordingly, the rate limiting step of the iron ore reduction would be the solid carbon gasification reaction, which indeed has relatively high activation energy [43]for fossil carbon. On the other hand the activation energy for reaction of iron ore with CO reported in the literature can be as low as 30–53 kJ/mol [46]. However, also for carbon gasification, kinetics depend on the structure of the solid carbon material.

In the present work the carbon material is the biochar produced during the early stage of heat up, whose gasification reactivity is expected to be higher than that of more graphitic carbons. Values of activation energy of 127 and 171 have been reported for gasification of Miscanthus chars [47], prepared at 600 °C and 800 °C, respectively. Indeed, more severe heat treatment of the biochar can induce thermal annealing [48] with subsequent loss of reactivity, microstructural tranformations and changes in the kinetic parameters.

In Fig. 9, the Arrhenius plots obtained from TG tests in the KIO reduction domain at different MIS:KIO rations are compared with the Arrhenius plot obtained for reduction of KIO with 6.7 % of $H_2$ in a previous work [32]. As a matter of fact a detailed kinetic analysis carried out on KIO reduction with $H_2$ by non-isothermal thermogravimetric analysis revealed three stages of reaction with three values of activation energy depending on the temperature range: $E_a$ = 133 kJ/mol (T < 550 °C), $E_a$ = 33 kJ/mol (550 °C < T < 700 °C) and $E_a$ = 83 kJ/mol (T > 700 °C), which are related to the three reduction steps of KIO ($Fe_2O_3 \rightarrow Fe_3O_4 \rightarrow FeO \rightarrow Fe$) [49].

From the inspection of Fig. 9 it can be observed that from 750 °C to 900 °C the reduction of iron ore using $H_2$ (grey) as reducing agent is faster than reduction with MIS. However, at temperature higher than T > 900 °C, the trend is reversed suggested that the reduction of KIO using MIS results more rapidly than using $H_2$ at all weight ratios used.

### 3.6. Morphological investigation

Morphological investigation of samples at different MIS:KIO ratios treated at different temperatures with $N_2$ has been performed and SEM and EDX. Selected SEM micrographs of samples at weight ratio of 1:1 at 750 °C, 900°c and 1000 °C are reported in Fig. 10.

From the inspection of the Fig. 10 it can be noted that KIO particles reduced at 750 °C appear edgy and with rather smooth surface; however, porosity in these particles seems to be negligible. Furthermore, MIS particles treated up to 750 °C seem to retain the original morphology of the raw biomass (as reported in Fig. S4). Increasing the temperature from 750 °C to 1000 °C, a variation of the KIO particles' surface from smooth to rough is detected. Indeed, the particles contour becomes less edgy and at higher magnification longitudinal cricks become evident. At 1000 °C, some deposits with spherical shape are detected on the MIS surface.

EDX analysis, reported in Table 8, reveals that the spherical deposits with smooth surface (blue box) come from the biomass pyrolysis, while the rough spherical deposits (orange box) are an agglomerate of carbon and smaller particles of iron material.

Fig. 11 reports KIO particles treated at 1000 °C where an extensive development of porosity is observed with formation of a sponge-like microstructure; this morphological architecture has been observed even for KIO reduced with $H_2$ [32].

EDX metal maps reveal a re-distribution of contaminants in the iron particles after complete reduction at 1000 °C. Indeed, the accumulation of gangue elements, Si, forms spherical drops within the iron sponge-like microstructure architecture.

**Table 7**
Kinetic parameter of iron oxides reduction with biomass.

| *Kinetic parameters* | |
|---|---|
| $E_a$ kJ/mol | $k_0$ 1/min |
| 180 | $4.8 \cdot 10^6$ |

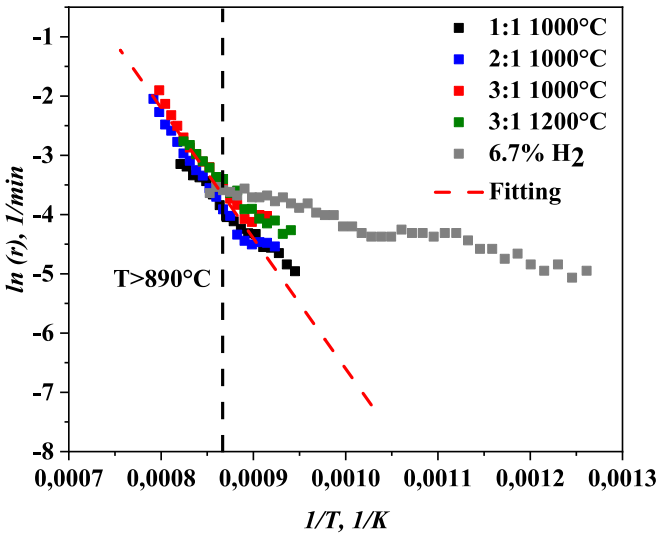


**Fig. 9.** Iron ore reduction kinetics with different weight ratio of biomass and with 6.7% $H_2$.

## 4. Conclusions

The present work reports the results of an experimental campaign of reduction of Khumani Iron Ore, using Mischantus Giganteous biomass as reducing agent, in controlled atmosphere, $N_2$, at different weight ratios and temperatures.

1. Biochar produced by biomass pyrolysis has been shown to be capable of reducing $Fe_2O_3$ to metallic iron. In particular, it has been shown that the reduction of $Fe_2O_3$ to metallic iron is not due to the volatiles generated during biomass pyrolysis but is due to the reaction between biochar and $Fe_2O_3$. Furthermore, it has been shown that increasing both the biomass to $Fe_2O_3$ ratio and the temperature increases the reduction degree of the following reaction $Fe_2O_3 \rightarrow Fe_3O_4 \rightarrow FeO \rightarrow Fe$. In particular, 90 % of crystalline phases composed of metallic iron have been obtained from the mixture composed of MIS:KIO 1:1 at 1000 °C which corresponds to iron sponge-like morphological architecture.
2. Based on mass balances, two different regions of temperatures have been identified: a) at T < 500 °C the mass loss is due to pyrolysis of biomass, b) at T > 500 °C the mass loss increases with the MIS:KIO ratio. The mass loss cannot be attributed only to the reduction of

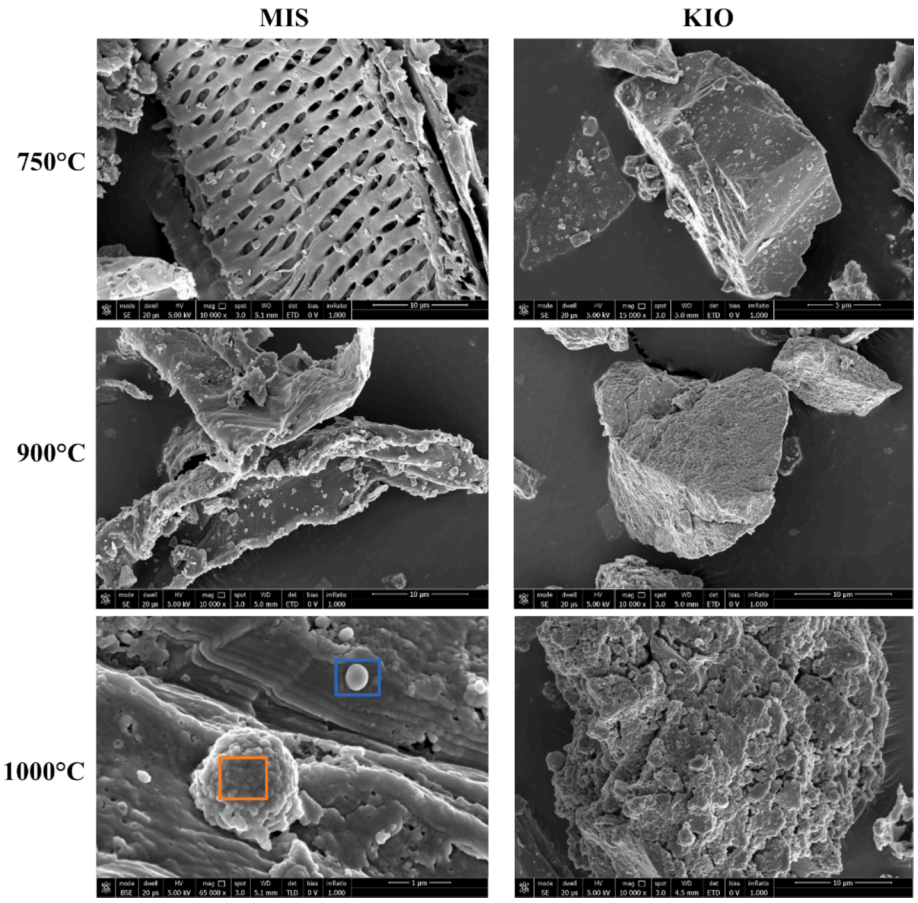


**Fig. 10.** SEM images of MIS:KIO 1:1 (wt%) treated at different temperatures.

**Table 8**
EDX analysis on selected spot on the surface of a biomass particle of 1:1 1000 °C sample.

| Element | Orange box (wt%) | Blue box (wt%) |
|---|---|---|
| Carbon | 32.7 | 89.6 |
| Oxygen | 18.7 | 6.7 |
| Iron | 41.6 | 1.6 |
| Silicon | 5.7 | 1.7 |
| Aluminium | 1.3 | 0.4 |

$Fe_2O_3$, but also biomass gasification occurs. This is evident in the appearance of remarkable CO peaks above 900 °C.

3. It is shown that kinetics of biomass pyrolysis at T < 500 °C is not influenced by the presence of KIO. Kinetics of KIO reduction has been obtained fitting the mass loss data above T > 750 °C.

In conclusion, our findings suggest that biochar fabricated by biomass pyrolysis is an alternative promising reducing agent for the reduction of a desired iron-based materials, from magnetite to metallic iron, in the ironmaking industry; however, further investigations will be carried out on the condensable volatiles.

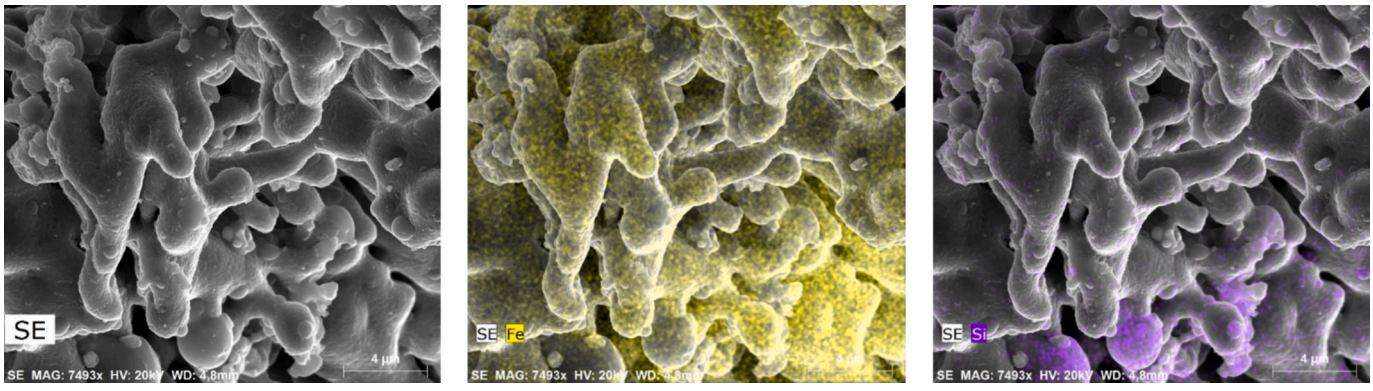


**Fig. 11.** SEM micrographs and EDX metal maps of KIO particles treated at 1000 °C.

## CRediT authorship contribution statement

**Antonio Fabozzi:** Writing – review & editing, Writing – original draft, Visualization, Validation, Supervision, Investigation, Formal analysis, Data curation, Conceptualization. **Francesca Cerciello:** Writing – review & editing, Writing – original draft, Methodology, Investigation, Formal analysis. **Osvalda Senneca:** Writing – review & editing, Writing – original draft, Visualization, Validation, Supervision, Project administration, Methodology, Investigation, Formal analysis, Data curation, Conceptualization.

## Declaration of competing interest

The authors declare that they have no known competing financial interests or personal relationships that could have appeared to influence the work reported in this paper.

## Acknowledgements

Antonio Fabozzi acknowledges funding from the European Union - NextGenerationEU under the National Recovery and Resilience Plan (PNRR), Mission 04 Component 2 Investment 3.1, Project "ECCSELLENT - Development of ECCSEL-R.I. ItaLian facilities: usEr access, services and loNg-Term sustainability" Code: IR0000020 - CUP F53C22000560006.

iENTRANCE@ENL - Infrastructure for ENergy TRAnsition aNd Circular Economy @ EuroNanoLab" - Code IR0000027 – CUP B33C22000710006 –European Union - NextGenerationEU under the National Recovery and Resilience Plan (NRRP), Mission 04, Component 2, Investment 3.1.

The authors acknowledge Antonella Giarra for the SEM investigations, Luigi Stanzione and Andrea Capuozzo for XRF analysis.

## Appendix A. Supplementary data

Supplementary data to this article can be found online at https://doi.org/10.1016/j.fuel.2024.133976.

## Data availability

Data will be made available on request.

## References

[1] Alper K, Tekin K, Karagöz S, Ragauskas AJ. Sustainable energy and fuels from biomass: a review focusing on hydrothermal biomass processing. Sustainable Energy Fuels 2020;4(9):4390–414.
[2] Abbasi T, Abbasi SA. Biomass energy and the environmental impacts associated with its production and utilization. Renew Sustain Energy Rev 2010;14(3):919–37.
[3] Adeleke AA, Ikubanni PP, Emmanuel SS, Fajobi MO, Nwachukwu P, Adesibikan AA, et al. A comprehensive review on the similarity and disparity of torrefied biomass and coal properties. Renew Sustain Energy Rev 2024;199:114502.
[4] Vassilev SV, Vassileva CG, Vassilev VS. Advantages and disadvantages of composition and properties of biomass in comparison with coal: An overview. Fuel 2015;158:330–50.
[5] Chen L, Wen C, Wang W, Liu T, Liu E, Liu H, et al. Combustion behaviour of biochars thermally pretreated via torrefaction, slow pyrolysis, or hydrothermal carbonisation and co-fired with pulverised coal. Renew Energy 2020;161:867–77.
[6] Kambo HS, Dutta A. Strength, storage, and combustion characteristics of densified lignocellulosic biomass produced via torrefaction and hydrothermal carbonization. Appl Energy 2014;135:182–91.
[7] Nurdiawati A, Zaini IN, Wei W, Gyllenram R, Yang W, Samuelsson P. Towards fossil-free steel: Life cycle assessment of biosyngas-based direct reduced iron (DRI) production process. J Clean Prod 2023;393:136262.
[8] Fabozzi A, Cerciello F, Senneca O. Reduction of Iron Oxides for CO2 Capture Materials. Energies 2024;17(7):1673.
[9] Suopajärvi H, Kemppainen A, Haapakangas J, Fabritius T. Extensive review of the opportunities to use biomass-based fuels in iron and steelmaking processes. J Clean Prod 2017;148:709–34.
[10] Mayyas M, Nekouei RK, Sahajwalla V. Valorization of lignin biomass as a carbon feedstock in steel industry: Iron oxide reduction, steel carburizing and slag foaming. J Clean Prod 2019;219:971–80.
[11] Battle T, Srivastava U, Kopfle J, Hunter R, McClelland J. The direct reduction of iron. Treatise on process metallurgy. Elsevier 2024:89–149.
[12] Coppola A, Scala F. Chemical looping for combustion of solid biomass: a review. Energy Fuel 2021;35(23):19248–65.
[13] Aboelela D, Saleh H, Attia AM, Elhenawy Y, Majozi T, Bassyouni M. Recent advances in biomass pyrolysis processes for bioenergy production: optimization of operating conditions. Sustainability 2023;15(14):11238.
[14] Briens C, Piskorz J, Berruti F. Biomass valorization for fuel and chemicals production–A review. Int J Chem React Eng 2008;6(1).
[15] Fahmy TY, Fahmy Y, Mobarak F, El-Sakhawy M, Abou-Zeid RE. Biomass pyrolysis: past, present, and future. Environ Dev Sustain 2020;22:17–32.
[16] Mathieson J, Somerville M, Deev A, Jahanshahi S. Utilization of biomass as an alternative fuel in ironmaking. Iron Ore Elsevier 2015:581–613.
[17] He L, Li S, Lin W. Catalytic cracking of pyrolytic vapors of low-rank coal over limonite ore. Energy Fuel 2016;30(9):6984–90.
[18] Bru K, Blin J, Julbe A, Volle G. Pyrolysis of metal impregnated biomass: an innovative catalytic way to produce gas fuel. J Anal Appl Pyrol 2007;78(2):291–300.
[19] Liang S, Liao Y, Li W, Li C, Ma X. Enhanced stability of iron-nickel oxygen carriers in biomass chemical looping gasification by core-shell structure. Chem Eng J 2023;451:138964.
[20] Samprón I, de Diego LF, García-Labiano F, Izquierdo MT, Abad A, Adánez J. Biomass Chemical Looping Gasification of pine wood using a synthetic Fe2O3/Al2O3 oxygen carrier in a continuous unit. Bioresour Technol 2020;316:123908.
[21] Mishra B, Baliarsingh SK. Kinetics of iron ore reduction by coal and charcoal. 2008.
[22] Li X, Wei G, Wang H, Tian B, Zhu R, Wang Y. Kinetics of fe-containing solid waste reduction by carbonaceous materials in CO2 atmosphere: The cause of reducing agent burnout during direct reduction treatment. Fuel 2024;360:130509.
[23] Bagatini MC, Kan T, Evans TJ, Strezov V. Iron ore reduction by biomass volatiles. Journal of Sustainable Metallurgy 2021;7:215–26.
[24] Das D, Anand A, Gautam S, Rajak VK. Assessment of utilization potential of biomass volatiles and biochar as a reducing agent for iron ore pellets. Environ Technol 2024;45(1):158–69.
[25] Kinaev NN, Jak E, Hayes PC. Kinetics of reduction of lead smelting slags with solid carbon. Scand J Metall 2005;34(2):150–7.
[26] Lobo LS, Carabineiro SA. Kinetics and mechanism of catalytic carbon gasification. Fuel 2016;183:457–69.
[27] Guo D, Zhu L, Guo S, Cui B, Luo S, Laghari M, et al. Direct reduction of oxidized iron ore pellets using biomass syngas as the reducer. Fuel Process Technol 2016;148:276–81.
[28] Guo D, Li Y, Cui B, Chen Z, Luo S, Xiao B, et al. Direct reduction of iron ore/biomass composite pellets using simulated biomass-derived syngas: Experimental analysis and kinetic modelling. Chem Eng J 2017;327:822–30.
[29] Zulkania A, Rochmadi R, Hidayat M, Cahyono RB. Reduction reactivity of low grade iron ore-biomass pellets for a sustainable ironmaking process. Energies 2021;15(1):137.
[30] Zuo H-b, Hu Z-w, Zhang J-l, Li J, Liu Z-j. Direct reduction of iron ore by biomass char. Int J Miner Metall Mater 2013;20:514–21.
[31] Anderson E, Arundale R, Maughan M, Oladeinde A, Wycislo A, Voigt T. Growth and agronomy of Miscanthus× giganteus for biomass production. Biofuels 2011;2(2):167–83.
[32] Cerciello F, Fabozzi A, Yannakis C, Schmitt S, Narin O, Scherer V, et al. Kinetics of iron reduction upon reduction/oxidation cycles. Int J Hydrogen Energy 2024;65:337–47.
[33] Abd Halim MH, Mokhtar NAM, Masnan SSK, Talib NK, Jusoh AF, Saidin M. X-Ray Fluorescence (XRF) analysis of iron ore at ancient Kedah iron smelting site, Sungai Batu archaeological complex, Bujang Valley, Kedah, Malaysia. Heliyon 2023;9(4).
[34] Salucci E, D'Angelo A, Fabozzi A, Senneca O, Bellucci F, Francesca R, et al. Valorization of Iron (II) Oxalate Dihydrate Coming from Pickling Processes through Thermal Conversion. Materials 2024;17(18):4630.
[35] Shibata H, Arai Y, Suzuki M, Emi T. Kinetics of peritectic reaction and transformation in Fe-C alloys. Metall Mater Trans B 2000;31:981–91.
[36] Reddy DS, Chang H-H, Tsai M-Y, Chen I-G, Wu K-T, Liu S-H. Swelling and softening behavior of iron ore-spent mushroom substrate composite pellets during carbothermal reduction. J Mater Res Technol 2023;22:1999–2007.
[37] Soleymani AP, Panjepour M, Meratian M. The Effect of Temperature and Carbon to Hematite Ratio on the Formation of Cementite During the Couple of STMA and Partial Melting Processes. Metall Mater Trans B 2016;47:846–58.
[38] Böttger J, Eckhard T, Pflieger C, Senneca O, Muhler M, Cerciello F. Green coal substitutes for boilers through hydrothermal carbonization of biomass: pyrolysis and combustion behavior. Fuel 2023;344:128025.
[39] Battle T, Srivastava U, Kopfle J, Hunter R, McClelland J. The direct reduction of iron. Treatise on process metallurgy. Elsevier 2014:89–176.
[40] Bagatini MC, Zymla V, Osório E, Vilela ACF. Carbon gasification in self-reducing mixtures. ISIJ Int 2014;54(12):2687–96.
[41] Ahmed H, Viswanathan N, Björkman B. Isothermal reduction kinetics of self-reducing mixtures. Ironmak Steelmak 2017;44(1):66–75.
[42] Strezov V. Iron ore reduction using sawdust: Experimental analysis and kinetic modelling. Renew Energy 2006;31(12):1892–905.
[43] Coetsee T, Pistorius P, De Villiers E. Rate-determining steps for reduction in magnetite-coal pellets. Miner Eng 2002;15(11):919–29.
[44] Neto LR, Borgert CH, Grillo FF, de Oliveira JR, Coleti JL, Frizon TEA, et al. Sustainable steel production: Evaluating the reduction kinetics of iron ore self-reducing briquettes with eucalyptus charcoal. J Clean Prod 2024;457:142426.
[45] Moon J, Sahajwalla V. Kinetic model for the uniform conversion of self reducing iron oxide and carbon briquettes. ISIJ Int 2003;43(8):1136–42.

[46] Chen H, Zheng Z, Chen Z, Bi XT. Reduction of hematite (Fe2O3) to metallic iron (Fe) by CO in a micro fluidized bed reaction analyzer: A multistep kinetics study. Powder Technol 2017;316:410–20.
[47] Tian H, Jiao H, Cai J, Wang J, Yang Y, Bridgwater AV. Co-pyrolysis of Miscanthus Sacchariflorus and coals: A systematic study on the synergies in thermal decomposition, kinetics and vapour phase products. Fuel 2020;262:116603.
[48] Guizani C, Jeguirim M, Valin S, Peyrot M, Salvador S. The Heat Treatment Severity Index: A new metric correlated to the properties of biochars obtained from entrained flow pyrolysis of biomass. Fuel 2019;244:61–8.
[49] Hammam A, Li Y, Nie H, Zan L, Ding W, Ge Y, et al. Isothermal and non-isothermal reduction behaviors of iron ore compacts in pure hydrogen atmosphere and kinetic analysis. Min Metall Explor 2021;38:81–93.